J. Fluid Mech. (1974), *vol.* 66, *part* 4, *pp.* 689–705
Printed in Great Britain

Source–sink flows in a rotating annulus: a combined laboratory and numerical study

By D. A. BENNETTS AND W. D. N. JACKSON
Meteorological Office, Bracknell, Berkshire, England

(Received 6 September 1973 and in revised form 10 June 1974)

A general characteristic of rapidly rotating fluids is that accurate experimental measurements can only be made of the main (azimuthal) flow. The secondary flow is then usually deduced from theory, although this is often incomplete in the boundary regions where the secondary flow is of most interest.

In this paper we consider the case of source–sink flow between the porous walls of a rapidly rotating annular container and numerically integrate the full equations of motion in order to determine the complete structure of the secondary flow. The results are compared with the (approximate) analytic studies of Hide (1968) and Bennetts & Hocking (1973) to show the differences between the two approaches.

A defect of many previous numerical papers has been the inability to check the solution in the nonlinear case. To overcome this, new experimental measurements of the azimuthal velocity profile for a Rossby number of 0·238 have been obtained and these are compared with the numerical results.

1. Introduction

This paper is concerned with the motions produced in a rotating annular container when the inner wall acts as a uniform radial source and the outer wall as a sink. The general properties of such a system have been discussed by Hide (1968) and here we look especially at the secondary flow in the boundary-layer regions. This has been investigated by numerical integration of the Navier–Stokes equations.

The non-dimensionalized equations of motion for an incompressible homogeneous fluid moving with velocity $V\mathbf{u}$ relative to a uniform rotation $\Omega\mathbf{k}$ are

$$\partial\mathbf{u}/\partial\tau + R(\mathbf{u}.\nabla)\mathbf{u} + \mathbf{k}\times\mathbf{u} = -\nabla\phi + E\nabla^2\mathbf{u}, \tag{1.1}$$

$$\nabla.\mathbf{u} = 0, \tag{1.2}$$

where V is the maximum azimuthal velocity, $\phi = p/2h\Omega V$ (p being the specific volume multiplied by a modified pressure which includes the centrifugal terms), τ ($= 2\Omega t$) is a modified time and h is the height of the container. The two parameters E and R are defined by

$$E = \nu/2\Omega h^2, \quad R = V/2\Omega h, \tag{1.3}$$

where ν is the coefficient of kinematic viscosity. We also find it useful to define one further parameter, C, to measure the curvature of the annulus.

$$C = 2(b-a)/(b+a),$$

where a and b are the inner and outer radii respectively.

Motions in rapidly rotating fluids are characterized by values of E and R that are very much less than unity. In these cases the flow in the main body of the fluid can at most times only be determined by matching through the boundary layers which form on the walls of the container. The technique for dealing with these boundary layers is well established when one of the small parameters is multiplied by the most highly differentiated term, but there is no general method for other cases. Fortunately, however, there is usually some parametric region where one parameter is more important than the others and this gives us a basis from which to start a full analysis.

The equations can be solved analytically if the inertial terms are neglected, and an elementary scale analysis indicates that this can be done with negligible errors if $R \ll E^{\frac{1}{4}} \ll 1$. This is called the linear case and in the steady state fluid moves towards the outer cylinder entirely within Ekman layers on the top and bottom boundaries. It flows along the inner cylinder wall towards the Ekman layers in Stewartson layers of thickness $O(E^{\frac{1}{4}})$, with substructure on a scale $E^{\frac{1}{3}}$, and leaves the Ekman layers to move along the outer cylinder wall in similar layers. This motion produces an azimuthal circulation in the geostrophic interior which is in the opposite sense to the rotation, although of course much smaller. For a fuller description of the flow see Hide (1968). If, however, $1 \gg R \gg E^{\frac{1}{4}}$, errors $O(1)$ are present in the regions of high radial shear, and the inertial terms are no longer negligible. This is the nonlinear case.

Recent papers by Hide (1968), Barcilon (1970) and Bennetts & Hocking (1973) find that in the nonlinear case the boundary layer on the source thickens from $O(E^{\frac{1}{4}})$ to $O(R)$ while the sink layer thins to $O(R^{-1}E^{\frac{1}{2}})$. Hide used an assumed form of the velocity distribution in the layer in reaching these conclusions and then derived an approximate formula for the thickness of the two layers. He also compared his estimates of the azimuthal circulation in both the side-wall layers and the interior with experimental results and obtained good agreement. Barcilon (1970) obtained the main features of the flow in the two layers by deriving an approximate analytic expression for the solution of the governing equation. Both these methods used the linear Ekman condition throughout. The third paper, Bennetts & Hocking (1973), derives the nonlinear Ekman condition under the assumption that the flow in the Ekman layer has a local similarity form.

The concensus of these three papers is that on the source there is an inertial layer of thickness $O(R)$ in which the fluid emerging from the cylinder retains its angular momentum, thus preventing centrifugal instability. In this layer the fluid is sucked into the Ekman layers at the top and bottom and the inward momentum of the fluid outside the Ekman layers has been lost in a distance $0{\cdot}68R$ (Bennetts & Hocking 1973) from the wall. At this point the fluid still has a discontinuity in the gradient of the radial velocity which is smoothed out by a viscous shear layer. There is then a second region of thickness $O(R)$ in which the azimuthal velocity is adjusted by the influence of the Ekman layers until the interior geostrophic value is reached.

On the sink boundary the change is quite different. Here the layer remains dominated by viscosity, but is thinner than in linear theory, being of thickness $O(R^{-1}E^{\frac{1}{2}})$. Fluid is injected from the Ekman layers at the top and bottom boundaries and redistributed uniformly over the sink, at the same time gaining angular momentum to match the boundary. For very small R this process is controlled by the Ekman layers via geostrophic and viscous forces, but as R increases the Ekman layers only control the outer part of the sink layer, and the inner part, nearest the wall, is more dependent on matching the no-slip condition, via viscous and inertial forces, than in redistributing the fluid; see Hamel (1916). Bennetts & Hocking also found that there was a lower limit to the thickness of this layer at $R = 1{\cdot}34\,(2E)^{\frac{1}{2}}$, in the present notation. They suggested that this limit was imposed by mathematical difficulties encountered in the solution of their equations rather than by more fundamental physical reasons, and the present numerical results confirm that there is indeed a solution when $R > 1{\cdot}34\,(2E)^{\frac{1}{2}}$.

In the present paper numerical methods permit us to use the full equations of motion and the Ekman-layer suction is then evaluated directly, not parameterized as in the above papers. The numerical calculation was performed with the following parameters, which allow comparison with the experimental measurements:

$$\left.\begin{aligned} a = 5{\cdot}06\text{ cm},\quad b = 11{\cdot}76\text{ cm},\quad h = 5{\cdot}00\text{ cm},\\ \Omega = 0{\cdot}25\text{ rad s}^{-1},\quad \nu = 0{\cdot}0100\text{ cm}^2\text{ s}^{-1}.\end{aligned}\right\} \tag{1.4}$$

These are used throughout except for two cases: in §3, when a comparison is made with Hide's solution in the linear case, and in §4 when the present numerical results and previous analytic solutions are compared. In both these cases we put

$$a = 1005{\cdot}06\text{ cm},\quad b = 1011{\cdot}67\text{ cm}, \tag{1.5}$$

thus making curvature effects negligible.

The range of the investigation is $0 < R < 0{\cdot}4$. Above this the source layer fills much of the container and begins to affect the sink. The higher values of Ω necessary to prevent this (the source-layer thickness is inversely proportional to Ω) could not be achieved because of computer limitations on time, and the gap width could not be increased appreciably because of limitations in space.

The results of the integration are compared with linear theory in §3. Direct comparison is difficult owing to the different requirements for E, linear theory requiring it to be infinitesimally small and the numerical model requiring a boundary layer of finite size. However the comparison sheds some light on the boundary layers and provides a basis for studying the curvature effects. In §4 the Rossby number is increased to 3×10^{-2} and the appearance of the inertial terms is noted in the boundary-layer regions. A further increase to about 3×10^{-1} then allows the structure of the thick inertial layer on the source and the thin viscous-dominated layer on the sink to be seen. Similar behaviour of the boundary layers has been noted by Dunst (1972) in his investigation of angular-momentum exchanges in rotating fluids.

2. The numerical model

We define velocity components (U, V, W) with respect to cylindrical polar coordinates (r, θ, z) fixed in the rotating frame of reference. The pressure can then be eliminated from the Navier–Stokes equations and the equations governing the axisymmetric flow become

$$\frac{\partial V}{\partial t}+\frac{1}{r}\frac{\partial(\psi, V)}{\partial(r,z)} = -\frac{1}{r}\frac{\partial\psi}{\partial z}\left(2\Omega+\frac{V}{r}\right)+\nu\left[\frac{\partial^2 V}{\partial z^2}+\frac{\partial}{\partial r}\left(\frac{1}{r}\frac{\partial(rV)}{\partial r}\right)\right], \tag{2.1}$$

$$\frac{\partial\zeta}{\partial t}+\frac{\partial(\psi, \zeta/r)}{\partial(r,z)} = 2\frac{\partial V}{\partial z}\left(\Omega+\frac{V}{r}\right)+\nu\left[\frac{\partial^2\zeta}{\partial z^2}+\frac{\partial}{\partial r}\left(\frac{1}{r}\frac{\partial(r\zeta)}{\partial r}\right)\right], \tag{2.2}$$

$$-\zeta = \frac{1}{r}\frac{\partial^2\psi}{\partial z^2}+\frac{\partial}{\partial r}\left(\frac{1}{r}\frac{\partial\psi}{\partial r}\right), \tag{2.3}$$

where ψ is the stream function in the plane θ = constant and is defined by

$$U = -r^{-1}\,\partial\psi/\partial z, \quad W = r^{-1}\,\partial\psi/\partial r. \tag{2.4}$$

ζ is the vorticity $\partial U/\partial z-\partial W/\partial r$.

Inspection of the above equations shows that the integration need only be performed over half the container, the flow being symmetric about the mid-height, and the origin is chosen so that

$$a < r < b, \quad 0 \geqslant z > -\tfrac{1}{2}h. \tag{2.5}$$

The boundary conditions for ψ and V are then

$$\psi = (Q/2\pi h)f(-\tfrac{1}{2}h), \quad V = 0 \quad \text{at} \quad z = -\tfrac{1}{2}h, \tag{2.6}$$

$$\psi = (Q/2\pi h)f(z), \quad V = 0 \quad \text{at} \quad r = a, b, \tag{2.7}$$

where Q is the total volume of fluid passing through the container per second. Some discussion is however required to explain $f(z)$. Over much of the boundary $r = a, b$, $f(z) = z$, giving a constant radial inflow, but near the corner regions it must be modified so that the no-slip condition on the top and bottom boundaries is satisfied. Ideally we should like to let the pressure distribution on the vertical boundaries determine $f(z)$ for us but this introduces severe numerical stability problems and we are forced to specify the function initially. By trial and error a good function was found to be

$$f(z) = z+E^{\frac{1}{2}}\exp\{-E^{-\frac{1}{2}}(z+\tfrac{1}{2}h)\}. \tag{2.8}$$

This function was chosen as it gave a simple pattern of streamlines in the corner regions. Although there is no physical evidence to support this choice, some justification is obtained by considering the two extreme cases $\partial^2 f/\partial z^2 \ll S$ and $\partial^2 f/\partial z^2 \gg S$, where S is the expression for $\partial^2 f/\partial z^2$ obtained from (2.8). The details of the streamlines in these two cases are illustrated in figures 1 (*a*) and (*b*)

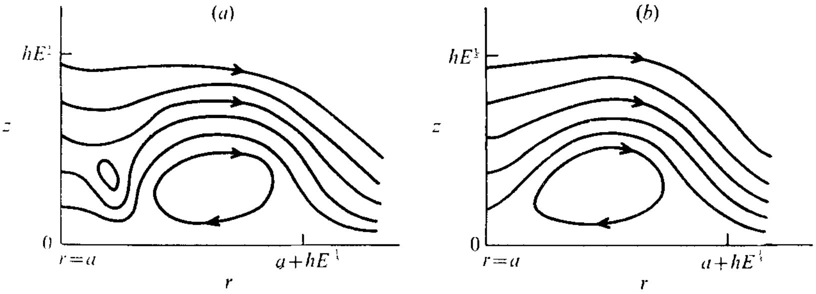

FIGURE 1. Sketches of the streamlines in the corner region (inflow wall) when (*a*) $\partial^2 f/\partial z^2 \ll S$ and (*b*) $\partial^2 f/\partial z^2 \gg S$. This pattern is preserved for the whole range of R and the disturbance was confined to a region approximately $E^{\frac{1}{2}}$ by $E^{\frac{1}{3}}$.

respectively. It was found that these patterns were preserved throughout the range of R and that the disturbance resulting from $\partial^2 f/\partial z^2 \neq S$ was confined to a region approximately $E^{\frac{1}{2}}$ by $E^{\frac{1}{3}}$.

Finally, we require the boundary conditions for ζ at the walls. These can be obtained by reversing the role of the Poisson equation, after Pearson (1965), which allows the introduction of the no-slip condition directly into the system. Pearson's formulae need to be modified slightly to account for the flow normal to the inner and outer walls, especially in the corner regions, but the change is straightforward and not presented here. The last boundary condition is that on ζ at $z = 0$ and by symmetry this is

$$\zeta = 0 \quad \text{at} \quad z = 0. \tag{2.9}$$

Finite-difference scheme

For a numerical solution of the (2.1) and (2.3) it is necessary to replace the continuous derivatives by their finite-difference analogues. The variables ψ, ζ and V are stored at uniformly spaced grid points in the plane θ = constant such that there are L spaces of length Δr and M of length Δz at times $n\Delta t$, where L, M and n are integers. L and M are then chosen by ensuring that the continuous derivatives and their finite-difference analogues differ everywhere by less than a prescribed amount, depending on the required accuracy of the solution. For problems in rotating fluids the choice of M reduces to ensuring that there are at least 3 grid points within the e-folding distance of the Ekman layer (Williams 1967) and a similar criterion can be applied for L. However, this gives more points than are required in the interior region where gradients are small and a more useful distribution can be obtained with a variable grid spacing, which has been used by many workers in recent years. Unfortunately stability considerations (see later in this section) require the time step, for an explicit method, to be governed by the minimum grid spacing. This would make it unacceptably small and require the use of implicit methods, which are both involved and time consuming in anything other than linear problems. For the particular parametric range under consideration this increase in complexity outweighs the saving of grid points. Since this would at most be 40 %, and in the more interesting nonlinear case only 20 %, the easier approach is used.

We use finite-difference operators $\delta_x\phi$, $\delta_{xx}\phi$ and Φ^x after Richardson (1922) and Lilly (1964), and (2.1)–(2.3) become

$$\delta_t\overline{V}^t + r^{-1}J_4(V) = r^{-1}(2\Omega + V/r)\,\delta_z\overline{\Psi}^z + \nu[\delta_{zz}V + \delta_r(r^{-1}\delta_r(rV))]^{\mathrm{lag}}, \tag{2.10}$$

$$\delta_t\overline{\zeta}^t + J_A(\zeta/r) = 2\Omega\delta_z\overline{V}^z + r^{-1}\delta_z(\overline{V}^2)^z + \nu[\delta_{zz}\zeta + \delta_r(r^{-1}\delta_r(r\zeta))]^{\mathrm{lag}}, \tag{2.11}$$

$$-\zeta = r^{-1}\delta_{zz}\psi + \delta_r(r^{-1}\delta_r\psi), \tag{2.12}$$

where central time differencing is used to ensure stability and the diffusion terms are evaluated non-centrally at time $(n-1)\Delta t$, again for stability. The terms J_4 and J_A are given by

$$J_4(\phi) = \delta_z(\overline{\phi}^z\delta_r\overline{\psi}^{rz}) - \delta_r(\overline{\phi}^r\delta_z\overline{\psi}^{rz}), \tag{2.13}$$

$$J_2(\phi) = \delta_r\overline{(\psi\delta_z\overline{\phi}^z)}^r - \delta_z\overline{(\psi\delta_r\overline{\phi}^r)}^z, \tag{2.14}$$

$$J_A(\phi) = \tfrac{2}{3}J_4(\phi) + \tfrac{1}{3}J_2(\phi), \tag{2.15}$$

where the multiple averaging is required to prevent fictional energy changes. For further details see Williams (1967) and Phillips (1959).

Provided that the spatial finite-difference scheme is well chosen there are given criteria for ensuring stability in time. The first is the diffusive requirement that the time step Δt must be less than $\min(\Delta z^2, \Delta r^2)/8\nu$. Second is the Courant–Friedrichs condition that no fluid particle can be advected more than a distance $\min(\Delta z, \Delta r)$ in a time Δt; this criterion is most important in the boundary layers where the velocities, in the plane $\theta =$ constant, are greatest. Finally, we must ensure that the energy of the inertial waves is not propagated at a speed greater than $\min(\Delta z, \Delta r)/\Delta t$. It is found that, provided that

$$\Delta t < (2^{\frac{1}{2}}/h)\min(\Delta r, \Delta z), \tag{2.16}$$

all three conditions are satisfied for the particular dimensions used. The tendency for central time differencing to lead to a slow splitting of variables at adjacent time steps is removed by periodically averaging.

Method of solution

In executing the calculations, V and ζ can be directly evaluated from values at the previous time step. With the new values of ζ and the known boundary conditions on ψ, the new values of ψ can be determined by the solution of Poisson's equation. This was achieved by a similar method to that of Williams (1967) by making use of the fast Fourier transform methods of storage allocation and flow diagrams given by the G–AE Subcommittee on Measurement Concepts (*Proc. I.E.E.E.* vol. AU-15, 1967, pp. 45–55). From the new values of ψ the boundary values of ζ could then be determined as described previously.

The integration is started with no inflow and the fluid in a state of solid-body rotation. The inflow is then built up over 5 s and thereafter held constant.The slow build-up was required as the grid was too coarse to represent the vorticity gradient adequately on the boundary if the whole of the fluid was impulsively started at $t = 0$.

Computational details

The most practical grid spacing, from the point of view of storage requirements and C.P.U. time, sufficiently small adequately to represent the flow was 66 × 81; 66 points in the vertical direction, when the end points are excluded, gives the required number for the inversion of Poisson's equation. It also gives 4 or 5 grid points within the Ekman-layer *e*-folding distance $(\nu/\Omega)^{\frac{1}{2}}$, and allows for the fact that the Ekman layer is expected to thin in some parametric regions. It is difficult to determine whether the grid spacing is sufficiently small for all parametric regions as the normal test of doubling and halving the grid spacing is denied us here. An increase to a 34 × 41 grid is suspect as there are then only about 2 grid points within the region of high shear; and we should not expect exact agreement with the grid with smaller spacing; it is impossible to halve this spacing because of storage limitations. Nevertheless a run was made with the larger grid spacing and changes of between 3 % and 7 % were encountered in the boundary layer.

With these parametric values the *e*-folding spin-up time is about 50 s (this will be discussed in the next section) and the model was run for about 300 s to get as near to a steady state as was practical. A run was also made to 400 s to check that a steady state had indeed been achieved. The values of the variable $-Vr$ for $R = 3{\cdot}05 \times 10^{-1}$ were 0, 0·4487, 0·6130, 0·6666, 0·6833, 0·6887, 0·6902, 0·6908 and 0·6910 at 50 s intervals up to 400 s. After 300 s the decay was exponential (to 4 significant figures), and given by

$$-Vr = 0{\cdot}6911\,[1 - 0{\cdot}5095\exp(-t/50{\cdot}0)], \tag{2.17}$$

the factor 0·5095 occurring because the initial part of the decay is not exponential. By terminating the integration at 300 s we therefore achieve 99·8 % of the final value.

The model requires 368 K of main storage and 200 K on direct access devices, and was run on an IBM 360/195.

3. The linear case ($R \ll E^{\frac{1}{4}}$)

As mentioned in the introduction, when $R \ll E^{\frac{1}{4}}$, we can solve (1.1) and (1.2) analytically by the boundary-layer technique given generally by Stewartson (1957) and more particularly for source–sink flows by Hide (1968). Briefly, Ekman layers form on the top and bottom surfaces and these transport all the fluid from the source to the sink. On the vertical walls, the fluid is transported to and from the Ekman layers by $E^{\frac{1}{4}}$ layers and we can formally write (away from the Ekman layers)

$$Vr = \frac{QE^{-\frac{1}{2}}}{2^{\frac{3}{2}}\pi h}\left[-1 + \exp\left(\frac{2^{\frac{1}{4}}E^{-\frac{1}{4}}(a-r)}{h}\right) + \exp\left(\frac{2^{\frac{1}{4}}E^{-\frac{1}{4}}(r-b)}{h}\right)\right], \tag{3.1}$$

$$Ur = \frac{Q}{2\pi h}\left[\exp\left(\frac{2^{\frac{1}{4}}E^{-\frac{1}{4}}(a-r)}{h}\right) + \exp\left(\frac{2^{\frac{1}{4}}E^{-\frac{1}{4}}(r-b)}{h}\right)\right], \tag{3.2}$$

where curvature effects have been neglected, i.e. $C = 0$. These expressions satisfy the boundary conditions on U and V, but examination of the continuity equation

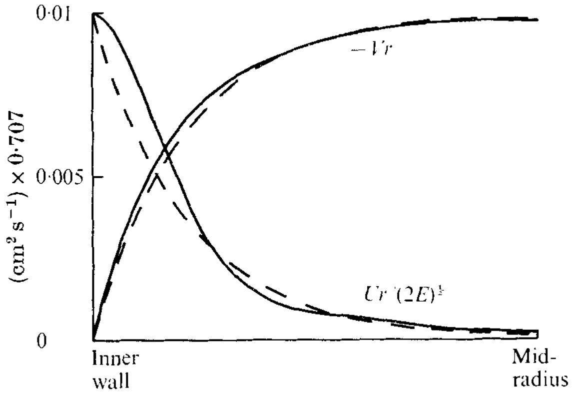

FIGURE 2. Comparison of Hide's linear theory (broken lines; $E = 8{\cdot}00 \times 10^{-4}$ but neglecting the $E^{\frac{1}{3}}$ layers) and the numerical results (solid lines) for $E = 8{\cdot}00 \times 10^{-4}, R = 3{\cdot}78 \times 10^{-4}$ and $C = 6{\cdot}64 \times 10^{-3}$.

shows that $W \neq 0$ near the vertical walls and the no-slip condition for W is not satisfied. This is corrected by an $E^{\frac{1}{3}}$ layer which also modifies the Vr profile by order $E^{\frac{1}{6}}$ and the Ur profile by a corresponding amount. Although the exact solution of this layer remains a significant unsolved analytic problem, numerically there are no special difficulties and we present here the solution when

$$R = 3{\cdot}78 \times 10^{-4}, \quad C = 6{\cdot}64 \times 10^{-3} \quad \text{and} \quad E = 8{\cdot}00 \times 10^{-4}.$$

The results of this integration are shown in figure 2 with expressions (3.1) and (3.2) plotted for comparison. It must be realized that these are now only approximate solutions but the comparison between them clearly brings out the contribution of the $E^{\frac{1}{3}}$ layer. Only half the profiles are given as both examples are symmetric about the mid-radius.

The Ur profile shows the most change since at all the wall $\partial(Ur)/\partial r$ is reduced from $O(E^{-\frac{1}{4}})$ to a small quantity (not zero as the finite-difference scheme is not accurate enough). On the other hand the viscous forces in the layer are considerably stronger than those in the $E^{\frac{1}{4}}$ layer (see figures 3c, d) and this allows a steeper Ur gradient away from the wall. The combination of these effects means that the overall thickness is little altered but the profile is substantially changed. There is a corresponding change in the Vr profile but the final values are almost the same, the numerical approach giving an 0·8 % lower value in the middle. (At this stage there is little indication of whether this difference is due to numerical error or is a real effect produced by the resolution of the $E^{\frac{1}{3}}$ layer.)

While still in the small Rossby number regime we also investigate the effects of curvature. E and R are kept at the same values as before but $C = 0{\cdot}76$ (experimental value). The results of this are given in figure 3. Figure 3(a) shows the Vr and Ur profiles, and these are to be compared with the numerical results in figure 2. On close inspection it is noticed that compared with the case

$$C = 6{\cdot}64 \times 10^{-3}$$

the source layer thickens and the sink layer thins (for the precise amount see table 1). The difference is small, about 2 % at a maximum, but can be under-

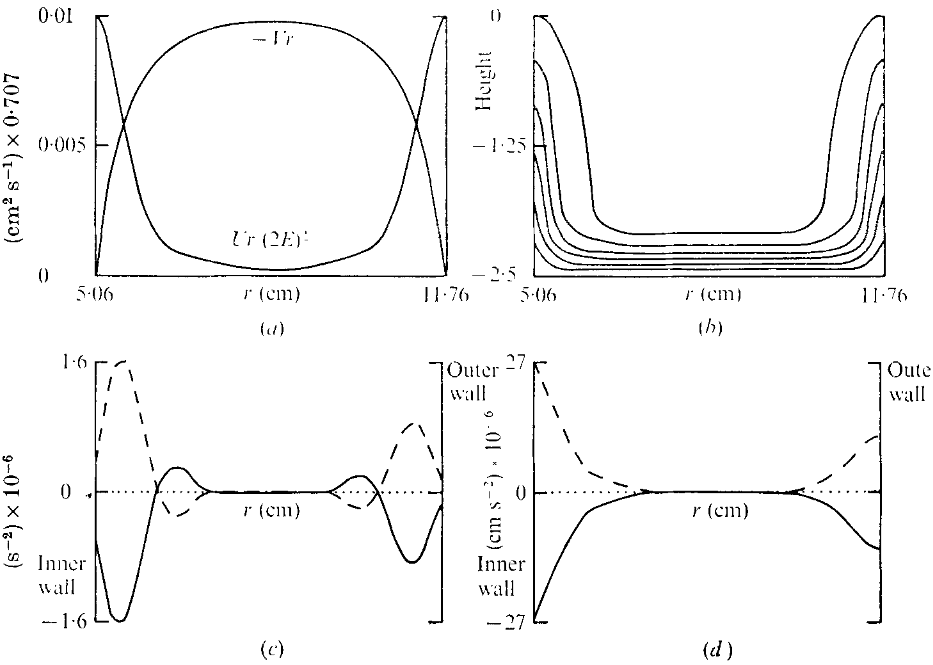

FIGURE 3. The results of the integration for $E = 8{\cdot}00\times10^{-4}$, $R = 3{\cdot}78\times10^{-4}$ and $C = 0{\cdot}76$. (*a*) Vr and Ur profiles. (*b*) Streamlines in the plane θ = constant for equispaced values of ψ: $\psi\times10^4 = 0{\cdot}55$, $1{\cdot}66$, $2{\cdot}76$, $3{\cdot}87$, $4{\cdot}97$ and $6{\cdot}07$. (*c*) Balance of terms for the vorticity equation. (*d*) Balance of terms for the V equation. (*a*), (*c*) and (*d*) relate to the mid-level of the fluid ($z = 0$) but are representative of all but the Ekman regions, which from (*b*) can be seen to be about 0·6 cm ($3(\nu/\Omega)^{\frac{1}{2}}$) thick. Curves in (*c*) and (*d*): ——, geostrophic term; – – –, viscous term; · · · · · ·, nonlinear term.

stood if we consider the r derivatives in the viscous term in the equations of motion:

$$\frac{\partial^2 V}{\partial r^2}+\frac{1}{r}\frac{\partial V}{\partial r}-\frac{V}{r^2}. \tag{3.3}$$

When $C \ll 1$ only the first term is important but as this is relaxed the curvature term $r^{-1}\partial V/\partial r$ becomes negative in the source layer, causing it to thicken, and positive in the sink layer, with the opposite effect. (In both layers $r^{-1}\partial V/\partial r \gg V/r^2$ in this parametric region, although of course if $C \gg 1$ the interaction of all three terms will have to be considered. It is important to note that the relative size of these two terms is dependent only on C and not on V.) Table 1 below summarizes the results of this section by giving the distances required for the various flows to reach 90 % of their maximum/minimum values.

Finally figure 3(*b*) gives the streamlines (for $C = 0{\cdot}76$) and figures 3(*c*) and (*d*) show the balance of the terms, away from the Ekman layer, in the vorticity and azimuthal velocity equations respectively. (The uniformity of the solution in the z direction is well known.) They clearly show the double structure of the boundary layer, the inner part being the $E^{\frac{1}{3}}$ layer superimposed on the weaker, outer $E^{\frac{1}{4}}$ layer. The corresponding values for the case $C = 6{\cdot}64\times10^{-3}$ are similar but there is no decrease in the amplitude of the terms near the outer boundary.

	Parametric values ($R = 3{\cdot}78\times10^{-4}$)	Source (cm)	Sink (cm)
Linear theory without $E^{\frac{1}{3}}$ layer	$E = 8{\cdot}00\times10^{-4}$ $C = 0$	1·64	1·64
Numerical results	$E = 8{\cdot}00\times10^{-4}$ $C = 6{\cdot}64\times10^{-3}$	1·47	1·47
	$E = 8{\cdot}00\times10^{-4}$ $C = 0{\cdot}76$	1·56	1·40

TABLE 1. Distances required for Vr and Ur to reach 90% of their geostrophic values for various values of E and C

Spin-up

We close this section with a brief note on the spin-up times of the model. Linear theory predicts an exponential decay which in the present case is given as $V_0[1-\exp(-t/50{\cdot}0)]$, V_0 being the final velocity. The spin-up of the numerical model can also be well approximated by an exponential curve and the best fit over the first 150 s for the interior region was

$$V_0[1-\exp\{-t/(50{\cdot}2\pm0{\cdot}3)\}]. \tag{3.4}$$

4. The nonlinear case ($1 \gg R \gg E^{\frac{1}{4}}$)

In the previous section we investigated the effects produced on flows of very small R by altering the curvature C. We now consider flows with larger R in which inertial forces become increasingly important. To isolate these effects E and C are left fixed at $8{\cdot}00\times10^{-4}$ and $0{\cdot}76$ respectively and we alter the inflow rate Q. Initially there is only a change in the scale of the velocities and it is not until the Rossby number becomes $O(10^{-2})$ that any noticeable effects occur. To investigate these a value $R = 3{\cdot}71\times10^{-2}$ is chosen, corresponding to an inflow 100 times that used in §3. Figures 4(a) and (b) show the results of the integration; for comparison see figures 3(c) and (d). The vertical boundary layers, previously involving a balance only of viscous and geostrophic terms, are seen to be modified and in the resulting layer there is a balance between all three terms. Why the effects are first observed in the inner part of the vertical boundary layer becomes apparent if we consider (2.1). Inertial effects are confined mainly to the Jacobian terms, and these are significant, compared with geostrophic terms, in the region of largest $\partial V/\partial r$, that is, the region of highest radial shear. Since only small changes are produced in the boundary-layer thicknesses, these have been shown in table 2 but figures corresponding to figures 3(a) and (b) have been omitted.

As the inflow rate is further increased the inertial forces increase and their influence spreads across the boundary layers. It is of interest to observe the different way in which the terms adjust to maintain the balance of the equations. On the source wall the geostrophic and inertial terms balance to almost conserve vorticity whilst on the sink all three remain of comparable magnitude. To study this case in detail a Rossby number of $3{\cdot}05\times10^{-1}$ is taken, corresponding to 10

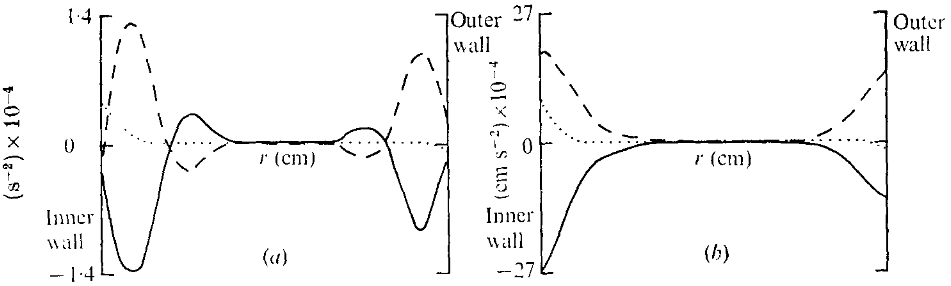

FIGURE 4. The results of the integration for $E = 8{\cdot}00 \times 10^{-4}$, $R = 3{\cdot}79 \times 10^{-2}$ and $C = 0{\cdot}76$. (*a*) Balance of terms for the vorticity equation. (*b*) Balance of terms for the V equation. Figures corresponding to figures 3(*a*) and (*b*) are omitted as, apart from scale, the profiles and streamlines are similar. Notation for curves as in figures 3(*c*) and (*d*).

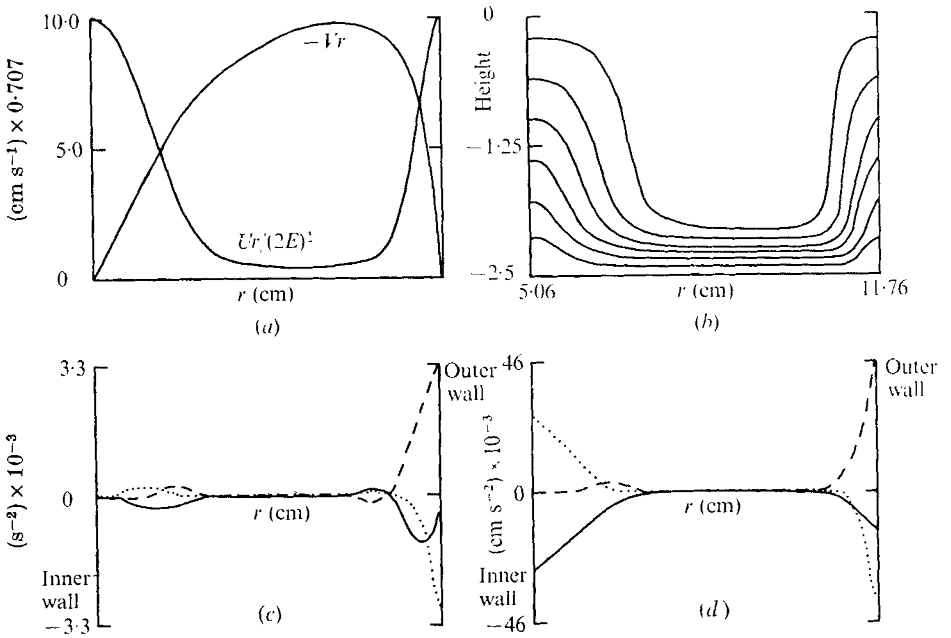

FIGURE 5. The results of the integration for $E = 8{\cdot}00 \times 10^{-4}$, $R = 3{\cdot}05 \times 10^{-1}$ and $C = 0{\cdot}76$. (*a*) Vr and Ur profiles. (*b*) Streamlines in the plane θ = constant for equispaced values of ψ: $\psi \times 10 = 0{\cdot}55$, $1{\cdot}66$, $2{\cdot}76$, $3{\cdot}87$, $4{\cdot}97$ and $6{\cdot}07$. (*c*) Balance of terms for the vorticity equation. (*d*) Balance of terms for the V equation. (*a*), (*c*) and (*d*) relate to the mid-level of the fluid ($z = 0$) but are representative of all but the Ekman regions, which from (*b*) can be seen to be very little thicker than in the linear case (figure 3). Notation for curves in (*c*) and (*d*) as in figures 3(*c*) and (*d*).

times the inflow of the previous run. The results of this integration are shown in figure 5. Figures 5(c) and (*d*) are plotted at the same value of z as figures 3(*c*) and (*d*), but this is not crucial for the comparison since even in this parametric region the solution departs only slightly from uniformity in the z direction.

Comparison of figures 3(*a*) and 5(*a*) shows the expected thickening of the source layer and thinning of the sink layer, but of special interest is the different

Rossby number	Source distance (cm)		Sink distance (cm)	
R	Vr	Ur	Vr	Ur
$3{\cdot}78\times10^{-4}$	1·56	1·56	1·40	1·40
$3{\cdot}71\times10^{-2}$	1·73	1·65	1·39	1·39
$3{\cdot}05\times10^{-1}$	3·18	2·35	0·82	1·17

TABLE 2. Summary of the distances required for Vr and Ur to achieve 90% of their interior (geostrophic) values

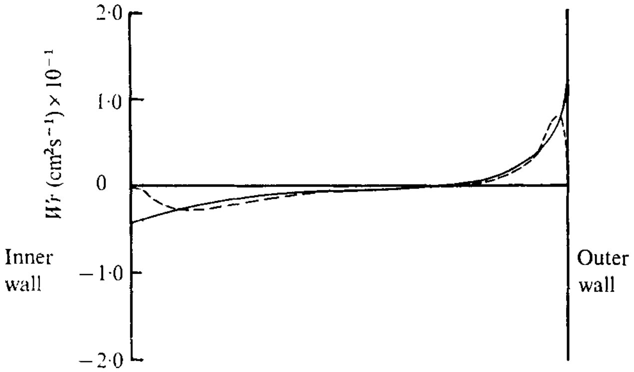

FIGURE 6. Change of Ekman-layer suction with radius as shown by Wr (for bottom boundary). The values are calculated at the edge of the Ekman layer at $z = -2{\cdot}0$. Unlike the numerical solution (dashed line), Hide's linear theoretical solution (solid line) does not fulfil the no-slip condition on the walls, owing to the neglect of the inner boundary layer.

distance that Ur and Vr require to reach 90% of their interior values. This difference was suggested by Bennetts & Hocking (1973) and was one of the major differences between the results of that paper and Hide (1968). A summary of these boundary-layer thicknesses is given in table 2.

In the source layer we can see from figures 5 (*a*) and 6 that the vertical velocity W and $\partial(Vr)/\partial r$ are still coupled, as in linear theory, indicating that the presence of inertial terms does not change the fundamental role of the Ekman layer. However, it will be noticed that the coupling between Vr and Ur is reduced; they no longer reach their geostrophic values in the same distance. This decoupling can also be seen from figures 5(*c*) and (*d*), where Ur is matched to the interior in an inner layer in which the inertial and geostrophic terms are balanced, the viscous terms remaining relatively small. The final match of Vr then takes place in an outer viscous–geostrophic layer. Both these layers are controlled by the Ekman layers as can be seen from figure 6, W being non-zero in each case. The magnitudes of the terms in the source layer (figure 5*c*) are very much less than those in the sink layer, indicating that near the source the vorticity is almost conserved. This is also demonstrated in figure 5(*d*), where the inertial–geostrophic balance of the inner layer is nearly

$$2\Omega + V/r = 0 \tag{4.1}$$

[see (2.1)]. This prevents centrifugal instability.

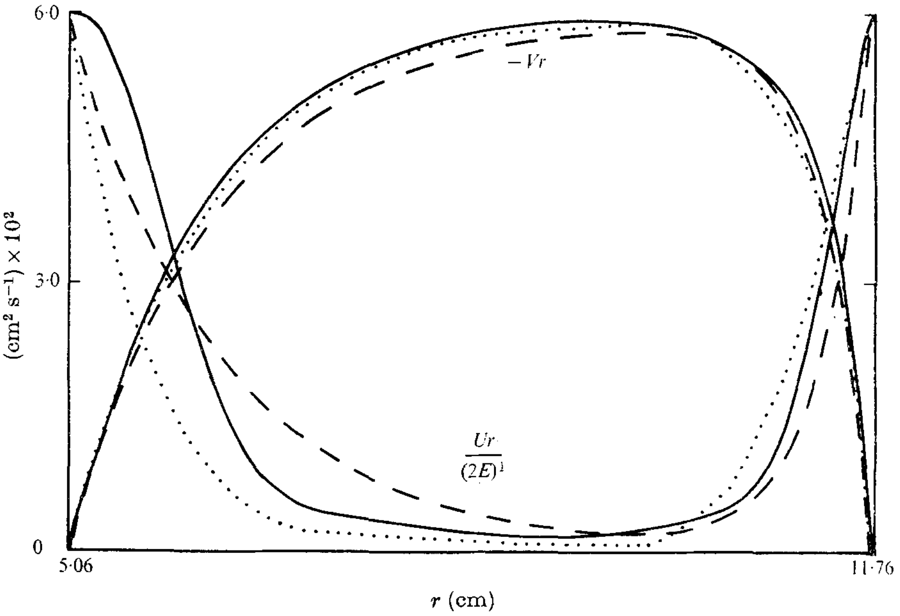

FIGURE 7. Comparison of the various results for $E = 8{\cdot}00\times10^{-4}$, $R = 2{\cdot}38\times10^{-1}$, $C = 6{\cdot}64\times10^{-3}$. ——, numerical results. Theoretical approaches, which neglect both curvature effects and the inner layer: ······, Bennetts & Hocking (1973); – – –, Hide (1968).

Turning our attention to the sink layer we again see a double structure in the boundary layer. However, because fluid is being forced onto this boundary its angular momentum must be increased. Since no purely inertial–geostrophic layer is capable of this increase, the layer thins to allow the viscous terms to become sufficiently large to balance the other two. Thus there is a change in character from the linear case in that the main balance is between viscous and inertial terms as opposed to viscous and geostrophic terms.

It is becoming noticeable, especially on the extreme left of figures 5(*c*) and 6 and on the graph of the streamlines, that a region is developing on the source boundary in which the fluid does not appear to feel the rotational constraints. The inflow velocity is sufficiently large to carry the fluid a measurable distance into the container in the one or two revolutions required for the Ekman layers to form on the top and bottom boundaries. In an analytic treatment this region could be represented as a quasi-time-dependent problem with the time coordinate replaced by $(r-a)/U$. However, from the numerical solution it is difficult to resolve the region with sufficient accuracy to confirm or disprove this hypothesis.

To compare the present approach with previous theories which neglect curvature terms, C is set equal to $6{\cdot}64\times10^{-3}$ and E and R are chosen as $8{\cdot}00\times10^{-4}$ and $2{\cdot}38\times10^{-1}$ respectively. The results are shown in figure 7. The solution of Hide (1968) gives reasonable agreement for the Vr profile but it is inherent in his original assumptions that the e-folding distances for Ur and Vr are the same. Consequently his Ur profile is poor. Bennetts & Hocking (1973) give slightly

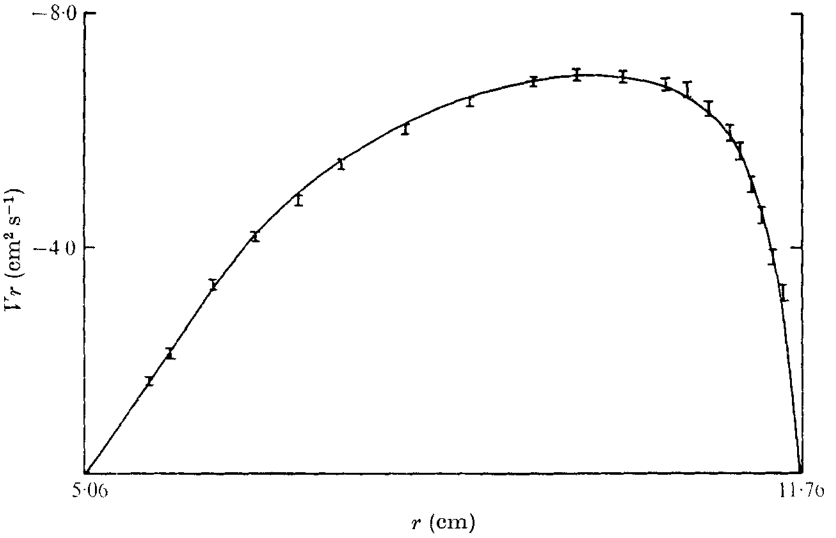

FIGURE 8. Comparison of the numerical and experimental results for parametric values $E = 8{\cdot}00 \times 10^{-4}$, $R = 3{\cdot}05 \times 10^{-1}$ and $C = 0{\cdot}76$. The experimental results are plotted with standard error bars.

	Numerical	Greenspan & Weinbaum	Wedemeyer
		Rossby number $= 3{\cdot}72 \times 10^{-2}$	
$(1-e^{-1})\,V_0$	$47{\cdot}0 \pm 0{\cdot}5$ s	47·8 s	46·8 s
$(1-e^{-2})\,V_0$	$92{\cdot}0 \pm 0{\cdot}5$ s	95·1 s	96·4 s
$(1-e^{-3})\,V_0$	$140{\cdot}0 \pm 0{\cdot}5$ s	142·3 s	146·2 s
		Rossby number $= 3{\cdot}05 \times 10^{-1}$	
$(1-e^{-1})\,V_0$	$47{\cdot}0 \pm 1{\cdot}0$ s	48·0 s	38·2 s
$(1-e^{-2})\,V_0$	$84{\cdot}0 \pm 1{\cdot}0$ s	90·5 s	84·1 s
$(1-e^{-3})\,V_0$	$126{\cdot}0 \pm 1{\cdot}0$ s	131·0 s	132·5 s

TABLE 3. The times taken for the fluid in the centre of the container to reach $(1-e^{-1})V_0$, $(1-e^{-2})V_0$ and $(1-e^{-3})V_0$, 63·2, 86·5 and 95·0% of the final velocity, as given by the numerical model, Greenspan & Weinbaum (1965) and Wedemeyer (1964)

better agreement, especially for the Ur profile, and predict the different e-folding distances of Vr and Ur. Nevertheless, these solutions fail near the boundaries because both assume that the inner layer is infinitesimally thin, a fact that is not possible to simulate computationally.

Finally, we make the comparison in the nonlinear regime between the numerical and experimental results. The parameters used are $E = 8{\cdot}00 \times 10^{-4}$, $C = 0{\cdot}76$ and $R = 3{\cdot}05 \times 10^{-1}$, and the Vr profile is plotted in figure 8. The agreement obtained, combined with the fact that we are using the full Navier–Stokes equations, gives us confidence in the predicted secondary flow.

Spin-up

In the previous section we noted agreement between the e-folding times of the model and theoretical predictions. As the Rossby number is increased there is a decrease in the e-folding times as shown in table 3 (V_0 is the final value of V at the mid-radius).

The theories of Wedemeyer (1964) and Greenspan & Weinbaum (1965) have been modified to account for the inflow. Since this has involved estimating the velocity fields after a time $O((2\Omega)^{-1}\,\mathrm{s})$ when the Ekman layers have formed, some differences in the values in the above table would be expected. Furthermore, it should be noted that for the numerical results the inflow was built up over 5 s whereas the theories assume an impulsive start.

5. The experimental measurements

The experimental measurements were made in an apparatus similar to that used by Hide (1968). This consisted of an annular region bounded at the top and bottom by flat acrylic (Perspex) plates and at the side by porous walls. It was desired to obtain measurements, particularly at higher Rossby numbers, which were more accurate and also more detailed in the side-wall layers than those previously available, and the azimuthal velocity component was selected for study since this velocity, at the mid-depth, was much larger than the radial or vertical velocities.

The rotating tank was made from an acrylic cylinder, whose ends were sealed by flat acrylic disks. Two concentric porous cylinders were placed inside this cylinder, forming an annular region through which fluid could be passed radially. These cylinders were made of sintered bronze (pore size 25 μm) and no noticeable 'jet effect', such as was noted by Hide (1968) when using a perforated source, was observed. They were carefully sealed to the acrylic lid and base of the apparatus to prevent flow around their edges, and their uniformity was checked by examining the radial flow of liquid while the tank was stationary. The size of the annular region so formed was of inside radius $5{\cdot}06 \pm 0{\cdot}02$ cm, outside radius $11{\cdot}78 \pm 0{\cdot}02$ cm and depth $4{\cdot}98 \pm 0{\cdot}03$ cm.

The tank was mounted on a rotating table with adjustable screws, which allowed the axis of the porous cylinders and the turntable to be aligned angularly to within $\pm 2 \times 10^{-3}$ rad and radially to within $\pm 0{\cdot}03$ cm. The turntable was driven by a synchronous induction motor, through a continuously variable transmission and a flat inelastic drive belt. The rotation period was measured by an electronic timer, triggered by a photocell, and was constant to within better than $0{\cdot}5\,\%$ over the length of a run.

The liquid used for these experiments was water, to which was added $0{\cdot}1\,\%$, by volume, of fresh milk to improve its light-scattering properties. This concentration did not appreciably affect the viscosity of the water, which was held constant at $0{\cdot}0100 \pm 0{\cdot}004\ \mathrm{cm}^2\,\mathrm{s}^{-1}$ by controlling its temperature. The water was supplied to the inner porous cylinder from a constant-head tank, passing through a needle valve and then onto the turntable through a fluid slip-ring.

After passing through the working region and the outer porous cylinder, the fluid flowed to waste over a constant-head outlet where the flow rate was measured to an accuracy of 0·5 % by timing the collection of a measured volume.

In order to obtain velocity measurements of higher accuracy and with less disturbance to the flow, the method of photographically timing the progress of dye markers, used in previous experiments, was discarded in favour of a laser-Doppler velocimeter system. These systems have been extensively discussed in the literature; see, for example, Durst, Melling & Whitelaw (1972) for a general review. In our case the whole system was required to rotate on the turntable above the working region and this dictated a unit which was compact, fairly light and relatively insensitive to vibration. Two parallel laser beams were produced by splitting the beam from a 1·5 mW helium–neon laser and these were focused to cross and form interference fringes in a measurement region of approximate size 0·02 × 0·02 × 0·30 cm. Light scattered forward by particles, of typical size 1 μm, passing through the fringes was reflected back through the focusing lens and collected on a photodiode, which produced a voltage whose mean frequency was proportional to the azimuthal velocity component of the fluid. All the optical components, except a plane mirror placed beneath the working region, were mounted in a rigid box which could move along a horizontal track. By turning a precision screw the intersection point of the beams could be moved radially through the working region and the measurement position determined to an accuracy of ± 0·01 cm. The signal from the photodiode was passed through an amplifier, a narrow-band filter and a squaring circuit before being measured by a frequency meter. Because of drop-outs of the signal, caused by the random passage of particles through the fringes, the whole system was calibrated by taking measurements in a small tank of fluid rotating as a solid body. The accuracy of measurements made with this system was 1 % at 8 cm s^{-1}, falling to 3 % at 0·3 cm s^{-1}.

All the measurements taken for this paper were made at a flow rate of 8·85 $cm^3 s^{-1}$ and at a rotation rate of 0·25 rad s^{-1}. The position of the intersection point of the laser beams was adjusted to be at the mid-depth of the working region and velocity measurements were made radially between the source and the sink. The mean results of several traverses are shown in figure 8 together with the r.m.s. deviations from the mean.

The authors would like to express their thanks to Dr R. Hide for suggesting this problem and for his continuing help, to Mr P. Brierley for constructing the turntable and to Mr R. O'Connor for his help in making the measurements. They would also like to thank the referees for their helpful comments. This paper is published with the permission of the Director General of the Meterological Office.

REFERENCES

BARCILON, V. 1970 *Phys. Fluids*, **13**, 537–544.

BENNETTS, D. A. & HOCKING, L. M. 1973 *Proc. Roy. Soc.* A **333**, 469–489.

DUNST, M. 1972 *J. Fluid Mech.* **55**, 301–310.

DURST, F., MELLING, A. & WHITELAW, J. H. 1972 *J. Fluid Mech.* **56**, 143–160.

GREENSPAN, H. P. & WEINBAUM, S. 1965 *J. Math. & Phys.* **44**, 66–85.

HAMEL, R. 1916 *Jber. dtsch. MatVer.* **25**, 34–47.

HIDE, R. 1968 *J. Fluid Mech.* **32**, 737–764.

LILLY, D. K. 1964 *J. Atmos. Sci.* **21**, 83–98.

PEARSON, C. E. 1965 *J. Fluid Mech.* **21**, 611–622.

PHILLIPS, N. A. 1959 In *The Atmosphere and the Sea in Motion.* (ed. B. Bolin), pp. 501–504. Oxford University Press.

RICHARDSON, L. F. 1922 In *Weather Prediction by Numerical Process*, p. 236. Cambridge University Press.

STEWARTSON, K. 1957 *J. Fluid Mech.* **3**, 17–26.

WEDEMEYER, F. H. 1964 *J. Fluid Mech.* **20**, 383–399.

WILLIAMS, G. P. 1967 *J. Atmos. Sci.* **24**, 144–161.